TITLE

A heterogeneous drug tolerant persister state in BRAF-mutant melanoma is characterized by ion channel dysregulation and susceptibility to ferroptosis

AUTHORS

Corey E. Hayford[1], Philip E. Stauffer[1], Blake Baleami[1], B. Bishal Paudel[1,2], Darren R. Tyson[3], Aziz Al'Khafaji[4,5], Kaitlyn E. Johnson[5], Leonard A. Harris[6,7,8], Amy Brock[4,5], and Vito Quaranta[3,9]

[1]Chemical and Physical Biology Graduate Program, Vanderbilt University School of Medicine, Nashville, TN USA
[2]Department of Biomedical Engineering, University of Virginia, Charlottesville, VA USA
[3]Department of Biochemistry, Vanderbilt University School of Medicine, Nashville, TN USA
[4]Institute for Cellular and Molecular Biology, University of Texas at Austin, TX USA
[5]Department of Biomedical Engineering, University of Texas at Austin, TX USA
[6]Department of Biomedical Engineering, University of Arkansas, Fayetteville, AR USA
[7]Interdisciplinary Graduate Program in Cell and Molecular Biology, University of Arkansas, Fayetteville, AR USA
[8]Cancer Biology Program, Winthrop P. Rockefeller Cancer Institute, University of Arkansas for Medical Sciences, Little Rock, AR USA
[9]Department of Pharmacology, Vanderbilt University School of Medicine, Nashville, TN USA

ABSTRACT

There is increasing interest in cancer cell subpopulations that can withstanding treatment via non-genetic mechanisms, such as tumor cell plasticity and adaptation. These cell populations may be comprised of cells with diverse phenotypes, e.g., quiescent or slow cycling. Such populations have been broadly termed "drug-tolerant persisters" (DTPs) and may be responsible for minimal residual disease following anticancer treatment and acquired resistance. Understanding molecular mechanisms that drive emergence of DTPs could lead to new strategies to improve therapeutic outcomes. Recently, we reported that BRAF-mutant melanoma cells under prolonged BRAF inhibition enter a DTP state with balanced cell death and division, which we termed "idling." Here, we apply single cell barcoding to show that idling DTP populations emerge via cell state transitions, rather than selection of a few pre-existing drug-tolerant clones. Within the time frame of our experiments, DTPs exhibit varying proportions of fast- and slow-cycling cells within each lineage, suggesting that entry into the DTP state is a stochastic process. Furthermore, single-cell transcriptomics and bulk epigenomics reveal common gene expression and ontology signatures in DTP lineages that are consistent with rebalancing of ion channels. Calcium flux experiments uncover a reduction of divalent cation reserves in intracellular organelles, likely leading to endoplasmic reticulum stress. Accordingly, idling DTPs are more prone to ferroptotic cell death, as indicated by increased sensitivity to inhibition of glutathione peroxidase 4 (GPX4), which prevents removal of toxic lipid peroxides. In summary, we propose that ion channel homeostasis is a central process underlying idling DTP emergence in BRAF-mutated melanoma. Future studies will investigate translational aspects of this insight.

INTRODUCTION

Cancer is a complex and dynamic disease characterized by intratumoral cell-to-cell variability that has been implicated in treatment evasion and acquired resistance to therapy.[1,2] Tumor cells exhibit multiple forms of variability, due to a complex interplay between genetics, epigenetics, and other non-genetic sources of variation.[3] Historically, genetic variability has received the most attention, with pre-existing or acquired genetic resistance mutations implicated as the primary cause of treatment resistance and tumor relapse. However, recently, epigenetic factors have become increasingly recognized as major sources of tumor heterogeneity and consequent treatment failure.[4–6] Epigenetic heterogeneity, defined as co-existence of multiple distinct phenotypes within a population of genetically identical cells,[6] may result in long-term drug tolerance, from which new genetic resistance mutations can ultimately arise.[7,8] As such, it has been suggested that a window of opportunity might exist between the onset of drug tolerance and the acquisition of genetic resistance mutations during which a targeted secondary treatment can be deployed to further reduce, or even eliminate, the residual tumor mass.[7,8] Accomplishing this will require a detailed understanding of the molecular drivers underlying drug tolerance so that potential vulnerabilities can be identified and exploited clinically.

Multiple investigators have reported cancer cell subpopulations capable of withstanding drug treatments via non-genetic mechanisms. These populations have been broadly termed "drug-tolerant persisters" (DTPs) and described, variously, as either quiescent[9] or slow cycling.[10–12] Recently, we described a similar drug-tolerant state, termed "idling," that arises in BRAF-mutant melanoma cell populations under prolonged BRAF inhibition.[7,13] Importantly, in contrast to previously reported DTPs, the idling phenotype refers to the state of a cell population, rather than of individual cells. More precisely, we found that the growth dynamics of drug-treated BRAF-mutant melanoma cell populations were best described by a model in which cells are distributed across multiple phenotypic states, each with a distinct proliferation rate.[7] In the idling state, cells are proportionally distributed across these states, such that the proliferation rate of the population as a whole is approximately zero. Given the significant interest in drug tolerance as a precursor to treatment failure and acquired resistance in tumors,[14] recognizing that DTP populations may, in fact, be heterogenous, composed of multiple phenotypic states that act collectively to evade and survive drug treatment, is crucial for developing effective treatment strategies against them.

Here, we demonstrate experimentally in BRAF-mutant melanoma that the idling phenotype is a heterogeneous collection of phenotypic states, which is less heterogeneous than the collection of states in untreated populations. This reduction in heterogeneity under drug pressure suggests idling cells may potentially be vulnerable to a targeted secondary treatment. Single-cell RNA sequencing demonstrates that idling populations comprise multiple distinct transcriptomic states that are more similar to each other than the states observed in untreated populations. Furthermore, we use DNA barcoding to show that the idling state is populated by cells from most lineages present in the untreated population, suggesting that phenotypic state transitions, rather

than clonal selection, underlies the establishment of drug tolerance. A gene ontology (GO) analysis, combining data from both transcriptomics and epigenomics, indicates that ion channel expression is significantly altered in idling cells relative to untreated cells, pointing to a role for mitochondrial metabolism in the idling phenotype. This is supported by calcium flux assays that show store-operated calcium entry (SOCE) is significantly altered in idling cells. Finally, idling cell populations are shown to have increased susceptibility to death by ferroptosis, supporting the notion that DTPs are vulnerable to targeted secondary treatments.

RESULTS

Drug-tolerant melanoma populations include cells from almost all untreated lineages

We have previously shown that BRAF-mutant melanoma cell lines exhibit non-linear drug response dynamics to BRAF inhibitor (BRAFi). The initial phase of drug response is characterized by variable degrees of proliferation rate reduction. This is followed by entry of the treated cell population into a state of near-zero proliferation rate, termed idling.[7] To determine whether the idling state populations are comprised of a collection of DTP clones, we barcoded the BRAF-mutant SKMEL5 melanoma cell line with a gRNA barcoding library.[15] This approach allowed for high-depth coverage of dynamics for multiple lineages in response to selective pressures (i.e., drug treatment) and the ability to distinguish between clonal selection and phenotypic state transitions (FIG. 1A). Upon treatment with BRAFi PLX 4720 (8 μM for 8 days), the barcode library complexity was reduced by less than 10% (FIG. 1B). These surviving barcodes were shared in a large majority of replicates within each condition (untreated and idling; FIG. 1C), as well as between conditions (FIG. 1D). These results indicate that most clonal lineages survive treatment and persist at a similar relative proportion after BRAFi treatment. Simply, the idling state consists of cells from an overwhelming majority of the untreated population, providing direct evidence against clonal selection in response to BRAFi.

Some fluctuations in relative barcode abundance do exist after treatment with BRAFi (FIG. 1E, see next section). The underlying fold change distribution for the entire barcoded cell population from untreated to idling is a normal distribution centered at zero, with no obvious exceptions; the top 25 most populous barcodes reflect this distribution and are used for downstream analyses (FIG. 1F). Notably, nearly all the lineages that do not survive treatment come from clones that have an exceedingly small representation in the overall distribution, suggesting that the loss of those lineages is due to random chance. These results indicate that phenotypic state transitions likely dominate the response to BRAFi, leading a diverse set of clonal lineages to adopt a phenotypic state(s) akin to DTPs.

Melanoma populations become less transcriptomically heterogeneous following prolonged BRAF inhibition

We performed single-cell transcriptomics on the barcoded cell line in untreated and in idling conditions (see Methods). Using Uniform Manifold Approximation and Projection[16] (UMAP) to project the transcriptomic profiles for all cells into two dimensions, we see that untreated and

130 idling cells clearly fall in different regions of the UMAP space, with minimal overlap (FIG. 2A).
131 Additionally, the idling cells reside in a more constrained region of the space, while in the
132 untreated cells two distinct clusters are evident.
133
134 To quantify the variability within and between populations, pairwise distances were calculated
135 between cells in each condition (FIG. 2B). Nearly all idling cells fall closer to one another than
136 untreated cells fall to each other in the principal component analysis (PCA) space using 10
137 principal components. The Earth Mover's Distance (EMD) was calculated between the two
138 pairwise distance distributions (EMD = 4.38) to measure the separation between the untreated
139 and idling populations. In summary, the untreated population is more heterogeneous than the
140 idling one in transcriptomic space.
141
142 Next, we aimed to determine the biological factors that differentiate the axes that separate
143 population clusters. UMAP_2 (e.g., separation between untreated clusters) largely separates
144 based on metabolic processes, consistent with our previous report of metabolic heterogeneity in
145 untreated melanoma cells[7] (Supplementary FIG. S1A). Specifically, the large untreated (UT_L)
146 cluster is enriched in a glycolysis gene signature compared to the small untreated (UT_S) cluster
147 (see Methods, Supplementary FIG. S1D). Conversely, the idling population is enriched in an
148 oxidative phosphorylation gene signature compared to both untreated clusters (Supplementary
149 FIG. S1D). This is consistent with multiple reports in the literature, where BRAF-mutant cells rely
150 primarily on glycolysis for growth and energy production, and BRAFi interferes with glycolytic
151 processes, presumably favoring a switch to oxidative phosphorylation (see Discussion).
152
153 Alternatively, UMAP_1 primarily separates based on cell cycle stage, even after cell cycle gene
154 signature regression, within the context of each cluster (Supplementary FIG. S1B). We used a
155 previously established cell cycle gene signature (see Methods) to classify individual cells by cell
156 cycle stage (G1, G2M, S). We then projected cell cycle stage on cells in the single-cell
157 transcriptomics UMAP space (FIG. 2C). For visualization clarity, cell cycle stages were simplified
158 into non-cycling (G1) and cycling (G2/M/S) states. The number and proportion of cells in cycling
159 vs. non-cycling states were calculated (FIG. 2D), and the number of cycling cells is dramatically
160 decreased in the treated population (67% vs 15%).
161
162 **Changes in barcode abundance between untreated and drug-tolerant populations can be**
163 **explained by simple random effects, not clonal selection**
164
165 The barcoding system we adopted integrates droplet cell barcodes with transduced gRNA lineage
166 barcodes, establishing a direct connection between the abundance of clonal lineages and their
167 location in the single-cell transcriptomics state space. The barcoding library was designed with a
168 relative low complexity (~65k potential barcodes, ~425 identified barcoded lineages), which
169 allowed for multiple instances of the same lineage barcode in gene expression space. We
170 projected the lineage distribution of SKMEL5 barcoded cells onto scRNA-seq UMAP space
171 (examples in FIG. 3A). Barcodes exhibit various UMAP transcriptomic state occupancies and fall
172 in both clusters (large and small) and cycling states across treatment conditions. In the untreated
173 clusters, barcodes tend to have an approximately similar breakdown between small and large

clusters as the average of the population. However, in the idling cell cluster, the breakdown between non-cycling and cycling cell states tends to be predictive of clonal lineage drug response (FIG. 1E; FIG. 3B). From these examples, three key behaviors emerge. The first is exemplified by barcodes 5 and 9, where only a few cells (~5%) from the barcoded cell lineages fall in the cycling idling state region of the cluster. This low proportion of cycling cells potentially leads to a reduction in the relative proportion of these barcodes post-treatment (FIG. 1E-F). The second behavior, as seen in barcodes 2 and 13, is the opposite, where an increased proportion of cells in each barcode fall in the idling cycling state (~23%). This increase in cells in the cycling state potentially leads to an increase in the relative proportion of both lineages after treatment (FIG. 1E-F). The third is characteristic of most lineages and falls somewhere in between, which causes a middling effect on treatment response (Supplementary FIG. S2). Thus, a strong correlation (Pearson, R=0.55) exists between the proportion of cells in the cycling idling state and the relative fold change of barcode abundance after treatment (FIG. 3C), indicating that this is a shared feature of all barcoded cell lineages.

Multi-omics analysis points to ion channel dysregulation as a central factor in drug tolerance

Due to the time scale of the appearance of DTPs, it is generally accepted that DTPs may arise by epigenetic regulation rather than the accumulation of mutations.[9–12] To determine whether this is the case for transitions to the idling state, we performed bulk ATAC-seq on SKMEL5 cells before and after BRAFi treatment (see Methods). In each condition, we identified a fragment size distribution characteristic of a successful run (Supplementary FIG. S3B; library complexity in Supplementary FIG. S3A). Regions of open chromatin were enriched in cells from both conditions, resulting in unique and shared peaks between conditions (see Methods; FIG. 4A). These peaks were normalized to the transcription start site (TSS), and the distribution of binding loci (Supplementary FIG. S3C) was used to quantify the peak feature set (FIG. 4B). Idling peaks have much fewer proximal features (e.g., promoter regions) and more distal elements (e.g., distal intergenic and intronic regions) compared to the untreated condition. Distal elements have been known to be involved in short-term epigenetic regulation. Unique peaks were also assigned to a corresponding gene, and genes associated with unique peaks were input into a GO over-representation analysis, which identified ion transport and activity as differentiators of idling (FIG. 4C).

To confirm this finding independently, we subjected clonal sublines[7] of SKMEL5 (SC01, SC07, and SC10) to bulk RNA sequencing (RNA-seq) over the course of BRAFi treatment (0, 3, and 8 days post-BRAFi). Even though these sublines have marked short-term differences in terms of BRAFi response,[7] they were chosen because they all converge to a long-term near-zero proliferation rate characteristic of idling (3-8 days). To understand the time evolution of clonal subline response to BRAFi, normalized counts of each subline were projected into reduced dimensionality space by PCA (FIG. 4D).

On day 0, prior to BRAFi treatment, sublines are distinct on the first PCA axis (PC1), with SC07 and SC10 showing the most similarity. In short-term treatment (day 0 → 3), sublines predominately change on PC2 and maintain the overall variance between sublines observed at

218 day 0 (FIG. 4D). In the long-term response (day 3 → 8), the sublines begin to converge on both
219 PC1 and PC2 (FIG. 4D). Considering that these three sublines are clonal derivatives of the SKMEL5
220 population, this result is consistent with the *en masse* transition of single cells to a common
221 UMAP space after treatment (FIG. 3A).
222
223 A differential expression analysis was performed between untreated (day 0) and idling (day 8)
224 across all three clones to identify transcriptomic signatures characteristic of idling. Differentially
225 expressed genes were input into a GO over-enrichment analysis to reveal processes upregulated
226 in the idling state. GO terms associated with ion transport and homeostasis were also found to
227 be upregulated in idling cells (MF – FIG. 4E; BP – Supplementary FIG. S3D; CC – Supplementary
228 FIG. S3E). In fact, statistically enriched GO terms shared a strong correlation between data
229 modalities, with the most significant terms pointing to the ion channel activity shown in previous
230 analyses (FIG. 4C and 4E). In summary, both epigenomics and transcriptomics data point toward
231 ion channel activity as a major molecular determinant of the idling state.
232
233 **Intracellular calcium ion flux is significantly reduced in drug-tolerant melanoma populations**
234
235 Next, we experimentally tested calcium channel activity in idling versus untreated cells, using a
236 calcium flux assay that measures the amount of ER resident calcium and propensity of SOCE
237 activity. In this assay, cyclopiazonic acid (CPA) is used to inhibit the activity of Sarcoendoplasmic
238 Reticulum Calcium ATPases (SERCAs), leading to a release of free calcium from the ER to the
239 cytoplasm where it is detected by the calcium dye, Fluo-8-AM. (first peak, FIG. 5A). To replenish
240 ER calcium upon depletion, cells undergo store operated calcium entry (SOCE) which brings in
241 extracellular calcium that can then be pumped into the ER by SERCAs. In order to isolate ER
242 calcium release from SOCE activity, CPA is added in a calcium free buffer, followed by addition of
243 calcium to the assay (second peak, FIG. 5A). ER calcium release stimulates the opening of plasma
244 membrane resident calcium channels (e.g., ORAI), but calcium cannot flow in until it is added to
245 the assay buffer, allowing ER calcium content/release and propensity of SOCE activity to be
246 studied separately. Idling cells exhibited decreased SOCE activity compared to untreated cells,
247 demonstrated by the second peak (FIG. 5A). These results verify differences in ion channel
248 activity in idling cells, and further suggest ER stress may be a vulnerability of idling cells.
249
250 To see if these differences in calcium flux may be a result of gene expression changes driven by
251 BRAFi treatment, a differential gene expression analysis was conducted on bulk RNAseq data
252 obtained from three SKMEL5 clonal sublines (FIG. 5B). Many of the queried calcium handling
253 genes are differentially expressed in sublines after 3 days and 8 days of BRAF inhibition.
254 Interestingly, trends in gene expression patterns seem relatively consistent across the sublines
255 (FIG. 5B). These results show that calcium handling genes are differentially expressed in cell
256 populations treated with BRAFi compared to untreated cell populations.
257
258 **Drug-tolerant melanoma populations exhibit increased susceptibility to death via ferroptosis**
259

Previous reports have indicated a connection between ion channels and ferroptosis, a type of regulated cell death, by way of increased ER stress.[17] Thus, induction of ferroptosis may provide a potential way to eradicate idling cancer cells. Indeed, expression of several genes in the ferroptosis signature is altered in melanoma cells upon BRAFi and entry into the idling state (FIG. 6A; Supplementary FIG. S4). Notably, glutathione metabolism gene expression is increased and genes for polyunsaturated fatty acid (PUFA) enzymes are decreased after BRAFi treatment, along with differences in various other parts of ferroptosis-related signaling. Interestingly, the expression pattern results in increased supply to the Fenton reaction, which produces the free radical precursors to reactive oxygen species (ROS), the step directly before commitment to ferroptosis (Supplementary FIG. S1E and S4).

To directly test susceptibility to ferroptosis, we subjected both drug-naïve and idling cells to treatment (see Methods) with RSL3; RSL3 is a compound that induces ferroptosis by targeting GPX4, a key regulator of glutathione oxidation and PUFA reduction. Interestingly, this treatment would reduce glutathione metabolism while preventing reduction of PUFA intermediates, leading to more precursors of the Fenton reaction and potentially to increased ROS that would drive cell death by ferroptosis. Interestingly, idling cells were ~3-fold more sensitive to RSL3 by potency (FIG. 6B; difference in IC50s), suggesting idling cells are susceptible to ferroptosis. Furthermore, addition of ferrostatin-1 (Fer-1), a drug that inhibits the production of lipid peroxides by the Fenton reaction (i.e., ROS), rescued the differential drug-response behavior of both idling and untreated cells in the presence of RSL3 (FIG. 6C). These results indicate that idling cells are vulnerable to ferroptosis, presumably due to the increased ROS that results from sequential GPX4 inhibition, providing a potential route to DTP elimination.

DISCUSSION

In this study, we show that BRAF inhibition (BRAFi) causes BRAF-mutant melanoma cells to transition *en masse* into idling populations of plastic drug-tolerant persisters (DTPs), which exhibit ion channel dysregulation and susceptibility to ferroptosis. Using cellular barcoding, we showed that idling cells result from an overwhelming majority of untreated clones, rather than clonal selection of a special idling clone (FIG. 1B-D). Distinct transcriptomic signatures were identified that differentiate untreated and idling cells, with the idling cells represented in a more restrained transcriptomic space (FIG. 2A-B). The idling cell population consisted of cells in cycling and non-cycling states, as defined by their phase in the cell cycle (FIG. 2C); though, the idling population had a lower proportion of cycling cells in its transcriptomic space than untreated cell populations (FIG. 2D). Barcoded clonal lineages were distributed across both transcriptomic states in the untreated condition (FIG. 3A). However, relative barcode abundances for lineages that have a larger proportion of cells in the cycling versus non-cycling idling state result in a larger proportion of that barcode in the idling population after treatment (FIG. 3A-C; c.f. FIG. 1E). Bulk epigenomics and time-series transcriptomics of the SKMEL5 cell line and clonal lineages identify a convergent idling molecular signature shared across modalities, which points towards ion dysregulation as a characteristic of the idling state (FIG. 4). The calcium ion channel dysregulation was validated in a calcium flux assay (FIG. 5A) and a differential gene expression analysis of ion channels (FIG. 5B). This evidence of calcium ion channel dysregulation further established a

potential connection to ferroptosis, a type of regulated cell death. A ferroptosis gene signature (FIG. 6A) suggested potential susceptibility to GPX4 inhibition through increased ROS; this susceptibility was validated to have a clear effect on idling cells (FIG. 6B). Rescue of the drugged phenotype by a lipid ROS scavenger verified the connection between idling drug tolerance and susceptibility to ferroptosis (FIG. 6C).

Many studies have remarked on the epigenetic plasticity as a way to understand decreased drug sensitivity,[18] and others have postulated using the epigenetic landscape as a mechanism to understand how cancer cells transition between states.[19] However, little experimental evidence exists showing how epigenetic state transitions lead to drug tolerance and eventual resistance. Together, these data provide evidence for a view of tumor cell plasticity where cells fall into basins across an epigenetic landscape. This study puts forth data that suggests a timeline for epigenetic plasticity of cancer cells prior to and after treatment. Tumor initiation from a single clone creates a population with the same genetic background. The genetic clone emanates an epigenetic landscape, comprised of several basins of attraction over which cells populate to create multiple cell types, each with different molecular phenotypes. Over time, cells in the landscape reach a dynamic equilibrium, i.e., cells can still transition between basins but the population is in a state of balance, a process known as “bet hedging”.[20,21] The introduction of a perturbation, such as an anticancer drug treatment, upends the equilibrated landscape and drops cells into a new landscape. Cells re-equilibrate to the new landscape and adopt cell fates corresponding to the state in which they now reside. In the case of a drug with good efficacy, most cells will fall into a state of the drug-treated landscape that results in death. However, if the new landscape includes a state where cells have a positive proliferation rate in drug, the population will invariably rebound. In our case, most of the cells matriculate into the large non-cycling state upon treatment with BRAFi, but some end up in a smaller cycling state (FIG. 2C). This feature is consistent with several different types of DTPs, from quiescent to slow-cycling.[9–12] However, some barcoded clonal lineages disproportionally fall into one of the two states (FIG. 3A), leading to a differential short-term drug fitness in response to BRAFi. Previous studies in the lab show that even sublines eventually adopt a near-zero proliferation rate in prolonged BRAFi,[7] suggesting that lineages fully equilibrate to the new landscape over time. This occurrence is largely consistent with other oncogene-addicted cancers treated with targeted therapies, which exhibit a noisy short-term drug tolerance that often leads to long-term genetic resistance.[22,23]

An actionable result of a drug-modified landscape is new biochemical network properties that can lead to new treatment sensitivities. This phenomenon, in which resistance (or tolerance) to one drug treatment confers sensitivity to a different drug (or drug class), is commonly known as “collateral sensitivity.” Interesting screens have been performed to identify drugs that have increased sensitivity for cells treated with an initial drug, including in cancer.[24] However, these methods ignore the heterogeneity present in treated populations and often lead to traditional up-front combination therapies. These combination therapies create an entirely new epigenetic landscape that has new molecular properties with unknown vulnerabilities,[6,25] making the new tumor difficult to treat. The heterogeneity identified in our idling cells exemplifies this problem and, therefore, requires a different approach. Sequential therapy is an alternative approach in which cells are able to equilibrate to the new drug-treated landscape with the hope that it is

348 more sensitive as a whole.[26] Molecular analyses in our study show that the drug-treated
349 landscape is indeed more homogeneous (FIG. 2A) and has a common thread in ion channel
350 activity across transcriptomics and epigenomics data (FIG. 4). By targeting the idling state with a
351 sequential therapy that leverages the increased ion channel activity to promote targeted
352 ferroptotic cell death, we seemingly create another epigenetic landscape where all of the basins
353 have a negative proliferation rate in drug treatment and result in tumor eradication. Therefore,
354 potential future studies could be aimed at identifying vulnerabilities of epigenetic landscapes
355 that result after primary drug treatment and finding patient-specific secondary drugs used for
356 sequential drug treatment regimens that eradicate the entire tumor. Together, these results
357 indicate that BRAF-mutant melanoma cells converge to a confined idling population after BRAFi
358 treatment, yet still exhibits cycling and non-cycling transcriptomic states. This breakdown
359 appears to encapsulate previously described DTPs that exhibit various cycling behaviors,
360 including quiescence, active division, and slow cycling.
361
362 **Figure captions**
363
364 **Figure 1: *Most clonal lineages survive treatment with BRAFi into idling.*** (A) Schematic of
365 example lineage tracing experiments using cellular barcoding. (B) Number of unique barcodes in
366 each treatment condition. Lines correspond to the means of three experimental replicates
367 (points). A minimum cutoff of 100 counts per million (CPM) was used. (C) Proportional sharing of
368 barcodes among experimental replicates (i.e., R1 = replicate 1) for each treatment condition. (D)
369 Heatmap of relative barcode abundances ($\log_{10}$ CPM) for each experimental replicates across all
370 captured barcodes. Heatmap is organized by decreasing barcode abundance in untreated
371 condition. (E) Relative fraction of the top 25 ranked (in untreated) barcoded cell lineages in
372 untreated and idling conditions. Bar height corresponds to the average of three experimental
373 replicates (line is standard deviation). (F) Distribution of ($\log_2$) fold change for barcoded clonal
374 lineages from untreated to idling. Means of fold changes were compiled into a distribution for all
375 captured lineages (grey), as well as the top 25 most abundant lineages noted in *E*.
376
377 **Figure 2: *Idling cells represent a convergent, yet still heterogeneous, transcriptomic state with***
378 ***less idling cells in the cycling state than untreated cells.*** (A) UMAP projection of untreated and
379 idling single-cell transcriptomes. 6410 cells are shown, with an approximately equal split between
380 conditions. (B) CDF of pairwise cell distances (random sampling of 15,000) with 10 principal
381 components on the PCA space of the untreated and idling single-cell transcriptomic data. An
382 Earth Mover's Distance (EMD) was calculated between the distributions to quantify their
383 separation from each other. (C) Overlay of cell cycle state (see Methods) on UMAP projection of
384 single cell transcriptomes (colored contours represent information in *A*)**.** (D) Relative proportion
385 of cells in cell cycle state for major untreated and idling clusters. The total number of cells in each
386 cluster (n) is noted above each bar.
387
388 **Figure 3: *Lineage distribution across cell cycle states is reflective of clonal dynamics.*** (A)
389 Projections of lineage transcriptomic distributions on UMAP projection in *FIG. 2A*. Lineages
390 correspond to colored dots, while contours reflect treatment condition. (B) Proportion of cells in
391 the idling cycling transcriptomic state for the top 25 most abundant barcodes. Dashed line

392 represents average of all barcodes. (C) A Pearson correlation analysis was performed between
393 the percentage of cycling cells in the idling state and the $\log_2$ fold change in barcode abundance
394 following BRAFi treatment for the top 25 most abundant barcodes.
395
396 **Figure 4:** ***Unique elements of the idling transcriptome and epigenome have differential features***
397 ***for ion activity.*** (A) Venn diagram of ATAC-seq identified peaks of open chromatin. (B) Alignment
398 of peaks to the TSS allows for prediction of epigenomic features.-Predicted feature distribution
399 in untreated, idling, or shared peaks. Peaks were assigned to features based on proximity to TSS
400 (see Methods). (C) GO over-enrichment analysis of genes associated to unique idling peaks. The
401 top 10 terms with the largest gene ratio are shown. (D) PCA projection of subclones (SC01, SC07,
402 and SC10) at multiple times (0, 3, and 8 days) in BRAFi. Each condition (e.g. SC01 at day 0) was
403 completed in triplicate. Lines are drawn between the centroids of triplicates across the time
404 series. (E) GO over-representation analysis on differentially expressed genes with increased
405 expression between untreated and idling. GO terms with the top 10 largest gene ratios (see
406 Methods) are shown.
407
408 **Figure 5:** ***Idling cells have decreased calcium flux and altered expression of calcium handling***
409 ***genes.*** (A) Calcium flux assay of untreated and idling cells using cyclopiazonic acid (CPA) to
410 deplete ER calcium without extracellular Ca^{2+}, addition of extracellular Ca^{2+} to test store operated
411 calcium entry (SOCE) activity, and ionomycin to control for number of cells in the assay. (B)
412 Differential gene expression analysis of calcium handling genes in sublines transcriptomics data
413 from *4D*.
414
415 **Figure 6:** ***Idling cell populations are susceptible to ferroptosis.*** (A) Gene expression values (z-
416 scores; see Methods) for multiple clonal sublines (SC01, SC07, SC10) across the BRAFi treatment
417 time course (0, 3, and 8 days post treatment). Genes are further grouped by their associated
418 processes related to ferroptosis. (B) DIP rate dose response curves for untreated and idling cells
419 treated with ferroptosis inducer RSL3. (C) Same as *B,* except with rescue experiments on the post-
420 treated cells using ferroptosis inhibitor Fer-1.
421
422 **Figure S1:** ***Analysis of the UMAP single cell transcriptomic space.*** (A) GO analysis of differentially
423 expressed between the untreated clusters in the UMAP single cell transcriptomics space shown
424 in *FIG. 2A.* (B) Same as *A* except the analysis was applied to the idling cluster and a subpopulation
425 of cells that were predominantly in the cycling state. (C) A representation of UMAP single cell
426 transcriptomic space of untreated and idling cells used for differential gene expression and GO
427 analyses in *D* and *E*. (D) Distributions of the signature scores for cells in each cluster in the
428 differential gene expression analysis from the GO analysis related to glycolysis and oxidative
429 phosphorylation. Colors of each distribution correspond to the colors of the clusters in *C*, where
430 pink is cluster 1 (i.e., UT_S), yellow is cluster 2 (i.e., UT_L), and blue is cluster 3 (i.e., idling). (E) Same
431 as *D* except with other processes.
432
433 **Figure S2:** ***Lineage distributions for barcodes with a middle effect in clonal dynamics to***
434 ***treatment response.*** Same as *FIG. 3A* for the remaining top 25 barcodes in the single cell
435 transcriptomics analysis.

436
437 **Figure S3:** ***Quality control of bulk epigenomics ATA-seq data and correlation analysis of***
438 ***differentially expressed genes in idling transcriptome and epigenome.*** (A) Plot of unique reads
439 versus sequenced reads for the bulk ATAC-seq data used in epigenome analyses. (B) Insert size
440 distribution of aligned reads from ATAC-seq data on untreated and idling cells. Both conditions
441 follow traditional nucleosome patterning. (C) Peak binding site distribution for untreated, idling,
442 and shared peaks. X-axis represents kb distances from the TSS. (D) Correlation analysis of the
443 differentially expressed genes from a Biological Process (BP)-type of GO analysis for the
444 epigenome and transcriptome of the idling cell population. (E) Same as *D* for a Cellular
445 Component (CC)-type of GO analysis.
446
447 **Figure S4:** ***Ferroptosis pathway*****.** A schematic diagram of the ferroptosis pathway with boxes that
448 correspond to the colors of the groups for the genes in *FIG. 6A*.
449
450 MATERIALS AND METHODS
451
452 **Cell culture and reagents**
453
454 We chose BRAF-mutant melanoma cell line SKMEL5 as a preferred model, since it exhibits median
455 BRAFi sensitivity compared to other BRAF-mutant melanoma cell lines.[27] SKMEL5 cell line was
456 purchased from ATCC© and labeled with either a fluorescent histone H2B conjugated to the
457 monomeric red fluorescent protein (H2BmRFP) and a cellular barcoding library (see "Cellular
458 barcoding" below) or H2B conjugated to the green fluorescent protein (H2B-GFP). Single cell-
459 derived subclones of SKMEL5 were selected and derived by limiting dilution, as described
460 previously. Cells were cultured in a mixed media of DMEM and Ham F-12 media (DMEM:F12 1:1;
461 catalog no. 11330-032), supplemented with 10% fetal bovine serum (FBS). Cells were incubated
462 at 37°C, 5% CO_2, and passaged twice a week using TrpLE (Gibco). Cell lines and sublines were
463 tested for mycoplasma contamination using the MycoAlert™ mycoplasma detection kit (Lonza),
464 according to manufacturer's instructions, and confirmed to be mycoplasma-free. BRAF inhibitor
465 PLX 4720 (analog to Vemurafenib), ferroptosis inducer RSL3 and ferroptosis inhibitor Fer-1 were
466 obtained from MedChem Express (Monmouth Junction, NJ) and solubilized in dimethyl sulfoxide
467 (DMSO) at a stock concentration of 10mM and stored at -20°C. Cell lines were originally stored
468 at -80°C, then moved into liquid nitrogen.
469
470 **Cellular barcoding**
471
472 *Setup:* Cellular barcoding library was constructed by cloning a guide RNA (gRNA) library of
473 barcodes into a CROP-seq-BFP-TSO vector as previously described. The vector was engineered
474 such that barcodes can be isolated by isolation and amplification (barcode sampling) or mRNA
475 capture in a single-cell RNA sequencing (scRNA-seq) experiment. gRNAs were built as a 20-
476 nucleotide sequence of four nucleotides identical among all barcodes, followed by a 16 strong-
477 weak (SW) paired nucleotides (i.e., XXXXSWSWSWSWSWSWSW). The SW pairing of the
478 barcode sequence was designed to prevent polymerase chain reaction (PCR) amplification bias.

479 The maximum complexity of this library is 2^{16} (~65,000 unique barcodes). The barcode library
480 vector was used to produce lentiviral libraries using a lipofectamine transfection of HEK293T
481 cells. Media containing lentiviral particles were collected at 48- and 72-hours post-transfection,
482 pooled, filtered through a 0.45 um Nalgene syringe filter and concentrated using a 50 mL size-
483 exclusion column by centrifugation at 2200 RCF at 4°C for two hours. Concentrated virus was
484 stored in -80°C. SKMEL5 cells were seeded in a 6-well plate at ~$1x10^6$ cells per well in 2.5 mL
485 culture media. Cells were transduced with the barcoded CROP-seq-BFP-TSO-Barcode_sgRNA
486 lentivirus using 0.8 μg/mL in each well and a multiplicity of infection (MOI) of 0.05. Twenty-four
487 hours after incubation, transduction media (containing polybrene) was exchanged for fresh
488 culture media. Forty-eight hours after incubation, barcoded cells were isolated by fluorescence-
489 activated cell sorting (FACS) and subsequently cultured until confluence in a T-150 dish and then
490 cryopreserved. Cryopreserved cells were thawed in a T-25 dish and scaled up for ~2 weeks in two
491 separate sets. The first set of thawed cells were treated with 8uM PLX4720 (and an untreated
492 control) for eight days and subjected to barcode sampling (see "Barcode Sampling Analysis"
493 subsection below). The second set was plated in three T-75 flasks (parallel replicates) and
494 independently treated with 8μM PLX4720 (or untreated control) for eight days and subjected to
495 scRNA-seq by the 10X genomics Chromium platform (version 2 chemistry; see "RNA single-cell
496 transcriptome sequencing" section below for more details). In both cases, treated cells had media
497 and drug replaced every three days. Untreated cells were expanded completely over the course
498 of the time course (i.e., no cell splitting).
499
500 *Barcode Sampling:* After PLX4720 treatment for eight days (or no treatment expansion), cells in
501 the first set were pelleted for genomic DNA (gDNA) extraction using the DNeasy Blood and Tissue
502 Kit (Qiagen) per manufacturers' instructions. Barcode sequences were amplified for each
503 replicate by polymerase chain reaction (PCR; 98°C for 30 seconds, followed by 22 cycles of
504 denaturation - 98°C for 10 seconds, annealing - 63°C for 30 seconds, extension - 72°C for 10
505 seconds, and a final extension of 72°C for 5 minutes) using primers containing flanking regions
506 and Illumina adapter index sequences. 2ug gDNA was used in each PCR reaction, and a
507 combination of 5 distinct pooled forward primers were utilized to minimize sequencing error.
508 Reactions were purified using a 1.8x AMPure XP bead (Beckman Coulter) cleanup. Reaction
509 products were confirmed using agarose gel confirmation (band at ~215bp). The resulting libraries
510 were quantified using a Qubit fluorometer (ThermoFisher), Bioanalyzer 2100 (Agilent) for library
511 profile assessment, and qPCR (Kapa Biosciences Cat: KK4622) to validate ligated material,
512 according to the manufacturer's instructions. The libraries were sequenced using the NovaSeq
513 6000 with 150 bp paired end reads as sequencing spike-ins (targeting ~200k reads). RTA (version
514 2.4.11; Illumina) was used for base calling and MultiQC (version 1.7) for quality control.
515
516 *Barcode Sampling Analysis:* Barcodes were identified from amplified sequence reads by trimming
517 flanking adapter sequences. Barcodes abundances were totaled and normalized to library read
518 depth, resulting in reads per million (RPM). Barcodes less than 100 CPM were removed from the
519 analysis. Numbers of unique barcodes were calculated based on this threshold. Overlaps
520 between experimental replicates were calculated to determine the proportion of barcodes
521 shared across different runs. Total barcode abundance (including low abundance barcodes) was

522 calculated using the log_{10} of barcode RPM for each replicate. Relative barcode fraction was
523 calculated for each sample across three replicates. Log_2 fold change of the idling to untreated
524 mean barcode fractions was calculated for all barcodes above the CPM threshold.
525
526 **RNA single-cell transcriptome sequencing**
527
528 *Data Collection:* After PLX4720 treatment for eight days (or no treatment expansion), cells in the
529 second set were prepared targeting ~3000 cells per sample, washed, and resuspended in 0.04%
530 bovine serum albumin (BSA) in phosphate-buffered saline (PBS). Cell suspensions were subjected
531 to 10X Genomics single-cell gene expression protocol (version 2, 3' counting) in two separate
532 wells, according to manufacturer's guidelines. Single-cell mRNA expression libraries were
533 prepared according to manufacturer instructions. Due to the nature of gRNA barcoding library
534 construction, mRNAs resulting from gRNA barcodes were captured along with other mRNAs.
535 Libraries were cleaned using SPRI beads (Beckman Coulter) and quantified using a Bioanalyzer
536 2100 (Agilent). The libraries were sequenced using the NovaSeq 6000 with 150 bp paired-end
537 reads targeting 50M reads per sample for the mRNA library (including barcode library). RTA
538 (version 2.4.11; Illumina) was used for base calling and MultiQC (version 1.7) for quality control.
539 Gene counting, including alignment, filtering, barcode counting, and unique molecular identifier
540 (UMI) counting was performed on each library using the *count* function in the 10X Genomics
541 software *Cell Ranger* (version 3.0.2) with the GRCh38 (hg38) reference transcriptome.
542
543 *Transcriptome Analysis:* Cell Ranger output two single-cell gene expression matrices, for
544 untreated and idling cells. scUniFrac was performed to quantify the degree of overlap between
545 conditions. Finding minimal overlaps, and since cells were prepared and processed in parallel, no
546 computational batch correction was performed. Seurat was used to perform gene expression
547 analysis. The *SCTransform* function was used to regress out mitochondrial gene expression
548 (percent.mt), number of features (genes; nFeature_RNA), number of RNA molecules in the cell
549 (nCount_RNA), and cell cycle variables (S.Score and G2M.Score). Feature selection was
550 performed according to Seurat guidelines using a variance stabilizing transformation of the top
551 2000 most variable features. Data was normalized and scaled according to Seurat guidelines.
552 Data between conditions were combined and visualized using the Uniform Manifold
553 Approximation and Projection (UMAP) dimensionality reduction algorithm as implemented in
554 Seurat. In addition to UMAP, t-distributed Stochastic Neighbor Embedding (t-SNE) and Principal
555 Component Analysis (PCA) were also performed, using the Seurat implementation. Clustering
556 was performed in the joint UMAP space using the default Seurat implementation, a shared
557 nearest neighbor (SNN) modularity optimization-based method. Pairwise Euclidean distances
558 were calculated between cells in each condition with 10 principal components in the PCA space
559 and plotted as a cumulative density function (CDF). An Earth Mover's Distance (EMD) was
560 calculated between 15000 randomly sampled pairwise distances using the *wasserstein1d*
561 function in the *transport* R package. Differential expression analysis was performed between
562 conditions (untreated, idling), between combined clusters (large, small) within each condition,
563 and between clusters across conditions (e.g., $untreated_{large}$ vs. $idling_{large}$). Differential expression
564 was performed using the Seurat *FindMarkers* function and DEGs (adjusted-p < 0.05) were input
565 into a GO over-enrichment analysis. The GO analysis identified cell cycle as a major factor

separating idling clusters and was not present for untreated clusters. Therefore, using cell cycle scores, a cell cycle phase (G1, G2M, S) was assigned to each cell, which was further simplified into cycling (S, G2M) and non-cycling (G1), which we call cell cycle state. Cluster proportion was calculated by cell cycle state to quantify the differences between clusters. The number of cells in each cell cycle state were tallied and calculated as a percentage across each cluster.

Barcode Analysis: After calculation of scRNA-seq gene expression matrices, barcode abundances were incorporated to the matrices. To do this, gRNA lineage barcodes had to be mapped to their associated 10X cell barcodes. First, unmapped scRNA-seq BAM files were cleaned to only include the mRNA transcript ID, scRNA-seq cell barcode, and scRNA-seq unique molecular identifier (UMI). Mapped scRNA-seq BAM files (3' heavy) were cleaned to only include the mRNA transcript ID and lineage barcode (from gRNA library). Unmapped and mapped subsets were merged on the mRNA transcript ID to assign a lineage barcode to each cell barcode and UMI. The resulting merged dataset was paired down to a single cell barcode – lineage barcode pair, which was appended to each cell in the gene expression matrix as a metadata tag. Barcode abundances were totaled across all cells in the experiment that captured a barcode, and strongly reflected barcode sampling relative abundances and fold changes upon treatment (FIG. 1E - scRNA-seq barcode fractions). Barcodes were overlaid on UMAP projections of scRNA-seq data, and further categorized into the cycling and non-cycling transcriptomic states (see Transcriptome Analysis subsection). Total number of cells from each barcode were tallied across each transcriptomic cell cycle state, and a percentage (relative to each barcode) in each state was calculated. A correlation analysis (Pearson) was performed on the percentage of cycling cells in idling vs. the $\log_2$ barcode fold change after treatment.

Functional interpretation analysis: The single-cell transcriptome count matrix (see "RNA single-cell transcriptome sequencing:Data Collection" above) was scaled by multiplying counts by the median RNA molecules across all cells and dividing that number by the number of RNA molecules in each cell (as recommended). Gene signature files were obtained from the molecular signatures database (MSigDB). *Hallmark* gene sets (50 in total) were downloaded from MSigDB (gsea-msigdb.org/gsea/msigdb/genesets.jsp?collection=H). Both the scaled counts matrix and each of the hallmark gene sets were input into VISION[28] to identify gene signature scores for each cell-signature pair. Four hallmark gene sets (KRAS_SIGNALING_UP, KRAS_SIGNALING_DOWN, UV_RESPONSE_UP, UV_RESPONSE_DOWN) were condensed into two (KRAS_SIGNALING, UV_RESPONSE) by VISION to leave 48 total gene signatures. Scores were compiled into a distribution and plotted by cluster (k=3) for each gene set.

Bulk RNA transcriptome sequencing

Data acquisition: Total RNA was isolated from untreated SKMEL5 single cell-derived subclones, each in triplicate, using Trizol isolation method (Invitrogen), according to the manufacturer's instructions. RNA samples were submitted to Vanderbilt VANTAGE Core services for quality check, where mRNA enrichment and cDNA library preparation were done with Illumina Tru-Seq stranded mRNA sample prep kit. Sequencing was done at Paired-End 75 bp on the Illumina HiSeq

609 3000. Reads were aligned to the GRCh38 human reference genome using 'HISAT2' and gene
610 counts were obtained using 'featureCounts'.
611
612 *Data analysis*: RNA-seq data was analyzed using the DESeq2[29] R package. Cells with less than 18
613 reads per condition were removed, according to DESeq2 vignettes. Counts were transformed
614 using the regularized logarithm (rlog) normalization algorithm. PCA was performed using the
615 *prcomp* function in R. The path between time series data points was visualized as a line between
616 subline-time point replicate means in the PCA space. EMDs were calculated between pairwise
617 distance distributions for each subline across the treatment time series and for each time point
618 across the sublines. Hierarchical clustering was performed using the *hclust* R function with a
619 Ward's minimum variance method. Differential expression analysis was performed using a model
620 design to quantify both changing variables and their interaction (~ subline + treatment time +
621 subline:treatment time). DEGs across sublines between untreated (pre-treatment, day 0) and
622 idling (day 8 post-treatment) were identified (adjusted-$p < 0.05$, log2 fold change > 2). DEGs were
623 input into a GO enrichment analysis, which identified GO terms associated with "Biological
624 Process" (BP), "Molecular Function" (MF), and "Cellular Component" (CC) GO types.
625
626 *Ferroptosis gene signature analysis:* A ferroptosis gene signature was obtained from the Kyoto
627 Encyclopedia of Genes and Genomes (KEGG). For each subline, genes were normalized to the 0-
628 day time point and a $\log_2$ fold change was calculated compared to the 0-day baseline. Groupings
629 of genes were annotated by separate signaling processes (Supplementary FIG. S5).
630
631 **Bulk ATAC epigenome sequencing**
632
633 *Data acquisition*: Data was collected using the omni-ATAC protocol for bulk ATAC sequencing
634 (ATAC-seq). After PLX4720 treatment for eight days (or no treatment expansion), cells in the
635 second set (in parallel to barcode sampling data collection) were pelleted at 50k cells and
636 resuspended in a cold ATAC-seq resuspension and lysis buffer containing NP40 (0.1%), Tween20
637 (0.1%), and Digitonin (0.01%) and incubated on ice. A resuspension buffer was added (0.1%
638 Tween20, no NP40 or Digitonin) to wash out the lysis reaction. Cells were pelleted and
639 resuspended in a transposition mix (5x Tris-DMF, PBS, 1% digitonin, 10% Tween20, nuclease-free
640 H_2O), including transposase Tn5, followed by a 30-minute incubation at 37°C, with shaking to
641 enhance tagmentation. After 30 minutes, the reaction was stopped by adding a DNA binding
642 buffer (Zymo) and purified using a DNA Clean and Concentrate kit (D4004, Zymo). The final
643 product was eluted in nuclease-free H_2O. PCR amplification was performed on the eluate with an
644 NEBNext 2X High Fidelity PCR Mix (NEB, M0541S) N7, and N5 index sequencing primers
645 (extension at 72°C for 5 minutes; denaturation at 90°C for 30 seconds; 12 cycles: denaturation at
646 98°C for 10 seconds, annealing at 62°C for 30 seconds, extension at 72°C for 30 seconds; final
647 extension at 72°C for 5 minutes). The PCR product was purified with the Zymo DNA Clean and
648 Concentrate kit and eluted in 22μL nuclease-free H_2O. ATAC-seq PCR libraries were visualized by
649 agarose gel electrophoresis for a quick check for the nucleosome ladder pattern (bands over ~150
650 bp). Libraries were also quantified using a Qubit fluorometer (ThermoFisher), Bioanalyzer 2100
651 (Agilent) for library profile assessment, and qPCR (Kapa Biosciences Cat: KK4622) to validate

652 ligated material, according to the manufacturer's instructions. The libraries were sequenced
653 using the NovaSeq 6000 with 150 bp paired-end reads as spike-ins on the sequencing chip
654 (untreated: ~160m, idling: ~130m reads). RTA (version 2.4.11; Illumina) was used for base calling
655 and MultiQC (version 1.7) for quality control.
656
657 *Data Analysis:* Reads were trimmed using *cutadapt* (paired-end) to remove primer sequences
658 and aligned to the hg38 reference genome using the *bwa mem* function in Burrows-Wheeler
659 Aligner (BWA, version 0.7.17). Aligned reads were sorted and duplicates were marked using
660 Picard (version 2.17.10). Untreated reads had more detected duplicates (~78% compared to
661 ~32% in idling). Reads were deduplicated, but to address the discrepancy in deduplicated library
662 complexity, idling reads were subsampled (25% of original library, Supplementary FIG. S4A-B) to
663 achieve a similar complexity to the untreated. Reads were further cleaned according to sequence
664 quality guidelines. Insert sizes were plotted from the output of *InsertSizeMetrics* after
665 deduplication in Picard. Peaks of open chromatin were called using the *MACS2 callpeak* function
666 according to recommended guidelines for ATAC-seq data (BAM paired-end method, q-threshold:
667 0.05, no MACS2 model, shift: -100, extension size: 200). Peaks were subjected to a further round
668 of quality control and cleaning using *ChIPQC* (peak mapping, peak duplication, blacklist peak
669 detection), and blacklisted peaks were removed. Peaks were converted to consensus counts
670 using the *runConsensusCounts* function in *soGGi*. Intersections of and unique cleaned peaks were
671 determined and visualized as a Venn diagram using the *vennDiagram* function in the *limma*
672 package. Unique and intersection peaks were annotated with the nearest neighbor genes using
673 the *annotatePeak* function and hg38 transcriptome in the *ChIPseeker* package. These peaks were
674 also re-aligned to the transcription start site (TSS) for each gene. Average profiles of read subsets
675 across all genes (nucleosome-free, mono-nucleosome, and di-nucleosome; normalized to the
676 TSS). Peaks were classified based on closeness to the TSS and assigned to predicted feature
677 (promoter, UTR, exon, intron, downstream, distal intergenic). Genes associated with unique and
678 intersections of peaks were input into a GO enrichment analysis for BP, MF, and CC GO types
679 (same as "Bulk Transcriptome Analysis" above). Transcription factor (TF) footprinting in the
680 region around TSSs was performed on untreated and idling unique peaks for key TFs.
681
682 **Gene ontology analysis**
683
684 *Setup:* Genes associated with unique ATAC-seq peaks (see "Bulk ATAC Epigenome Sequencing:
685 Data Analysis" above) were identified for each condition (i.e., untreated or idling). Additionally,
686 DEGs from the bulk RNA-seq statistical analysis were determined (8-day vs. 0-day time points
687 across all clonal sublines; see "Bulk RNA Transcriptome Sequencing:Data Analysis" above). The
688 two gene lists were independently subjected to a GO enrichment analysis using '*clusterProfiler*'.
689 Genes were compared to BP, MF, CC GO types. GO terms significantly enriched in the unique
690 ATAC-seq peaks ($p < 0.05$) and in DEGs ($p < 0.05$) were identified and stored independently as
691 separate GO term lists for untreated and idling datasets.
692
693 *Correlation Analysis:* The $-\log_{10}$(p-value) was calculated for terms shared between the lists
694 associated with the separate modalities, ranking terms based on statistical significance.

Spearman correlation was calculated between the significant GO terms using the *ggpubr* package (version 0.4.0) for each GO type.

Calcium flux assays

Data acquisition: SKMEL5 barcoded cells were plated onto a 384 well, tissue culture treated plate 24 hours before imaging at a density of 10,000 cells/well. For the treated condition, cells were treated with 8 µM PLX4720, a vemurafenib derivative, for 8 days with fresh media/drug swapped out every 3 days. Untreated control cells were taken from the same cell line culture which was maintained separately while the treatment condition was exposed to PLX4720, being split down when necessary to maintain healthy growth conditions. On the day of experimentation, the 384 well plate with all treated and untreated cells were incubated with 4 µM Fluo-8-AM in fresh culture media (10% FBS) for 1 hour at room temperature, as recommended by the manufacturer (AAT Bioquest). Dye containing media was removed and Hanks Buffered Saline Solution (HBSS, 10 mM HEPES, no Ca^{2+}) was used to wash the wells of excess dye, followed by removal and addition of 20 µL of fresh HBSS (no Ca^{2+}) for use as the assay buffer. The plate was loaded into a kinetic imaging instrument (Panoptic, by Waveguide Biosciences), which records the fluorescent intensity emitted by each well of the 384 well plate. A three-addition protocol was used to add the various drugs and assay conditions to the plate during the SOCE assay. Drug Addition plates were loaded with assay buffer (HBSS, with or without Ca^{2+}) and thoroughly mixed immediately before imaging. Add conditions were split into three parts: 1) Cyclopiazonic Acid (CPA; final concentration of 50 µM) to inhibit activity of Sarcoendoplasmic Reticulum Calcium ATPase (SERCA), leading ER Ca^{2+} release; 2) Addition of Ca^{2+} to the assay condition to activate SOCE activity; and 3) Addition of the Ca^{2+} ionophore, Ionomycin (final concentration of 5 µM), was used to generate maximal signal intensity to control for variations in cell count in individual wells (this was particularly important since drug treated idling cells experienced increased washout due to the stressful nature of sustained BRAF inhibition). Fluo-8-AM was excited with [480 nm] and imaged at [538 nm], with a frequency of 1 Hz. The CPA treatment condition was imaged for 260 seconds before addition of Ca^{2+}, followed by 270 seconds of imaging before addition of 5 µM Ionomycin. Treatment conditions were replicated in sets of 8 and average values traced with 95% confidence intervals.

Data analysis: Fluorescence data were normalized by dividing data from each well by the first fluorescence value at the start of the experiment. The ionomycin peak was used as a control for the number of cells in each treatment group, as the idling population tends to have less cell than the untreated population. Therefore, the mean ionomycin treatment peak was calculated for each treatment group (i.e., idling and untreated), and data from each treatment group were divided by the corresponding mean ionomycin peak value to account for the change in the number of cells in the assay. For comparison of calcium flux between the treatment groups, the lowest values were the zero starting point (on the y-axis) in the plot for each of the curves. A mean and 95% confidence interval were calculated for each time point and plotted using *ggplot*.

737 **Ferroptosis-induction experiments**
738
739 Plates of H2B-GFP-labeled SKMEL5 cells were treated with either vehicle (DMSO) or BRAFi (8μM
740 PLX4720) for eight days incubated at 37°C and 5% CO_2, changing media (with vehicle/drug) every
741 three days. BRAFi-treated cells were plated at ~2500 cells per well in a black, clear-bottom 96-
742 well plate (Falcon). After cell seeding, RSL3, with or without Fer-1, was added the following
743 morning, with media changes every three days (six replicates per condition). Plates were imaged
744 using automated fluorescence microscopy (Cellavista Instrument, Synentec). Twenty-five non-
745 overlapping fluorescent images (20X objective, 5x5 montage) were taken twice daily for a total
746 of 150 hours or until confluency. Cellavista image segmentation software (Synentec) was utilized
747 to calculate nuclear count (i.e., cell count) per well at each time point (Source = FITC, Dichro =
748 FITC, Filter = FITC, Emission Time = 800μs, Gain = 20x, Quality = High, Binning = 2x2). Cell nuclei
749 counts across wells were normalized to time of drug treatment and used to calculate a DIP rate
750 (stable linear growth rate). A dose-response curve was calculated across replicates using the *drm*
751 R package with a 4-parameter log-logistic function, with DIP rate as the drug effect. Replicates
752 were used to calculate means and 95% confidence intervals for the dose-response curves. IC_{50}
753 values were calculated for each condition and plotted as vertical dashed lines. Data was visualized
754 using the ggplot2R package (version 3.2.0).
755
756 **Model and Experimental Analysis Code Availability.** The codes used to generate model
757 simulations and analyze experimental data are publicly available via GitHub, or from the
758 corresponding author upon request.
759
760 **Data Availability.** The sequencing datasets generated in this study can be found in the gene
761 expression omnibus and sequence read archive. Additional experimental data will be available
762 from the corresponding author upon request.
763
764 ACKNOWLEDGEMENTS
765
766 We thank Emily Hodges and Kelly Barnett for ATAC-seq reagents and experimental advice. We
767 also thank Jing Hao for reagent acquisition and Tony Capra, Christian Meyer, Sarah Maddox
768 Groves, Carlos Lopez, Alissa Weaver, John McLean, Bruce Damon, and Ken Lau for useful
769 discussions.
770
771 Sequencing studies were performed by the Vanderbilt Technologies for Advanced Genomics
772 (VANTAGE) core facility at Vanderbilt University Medical Center with help from Angela Jones,
773 Karen Beeri, Jamie Roberson, Latha Raju, and Matthew Scholz. Cellular barcode library
774 construction and transduction were performed in the Brock laboratory at The University of Texas
775 at Austin. Data processing and model simulations were performed using resources at the
776 Advanced Computing Center for Research and Education (ACCRE) at Vanderbilt University.
777
778 This work was supported by the following funding sources: C.E.H., National Institutes of Health
779 (NIH) Ruth L. Kirschstein National Research Service Award (NRSA, F31-CA221147) and Chemical-
780 Biology Interface Training Grant (T32-GM0650); L.A.H., National Cancer Institute (NCI) Transition

Career Development Award to Promote Diversity (K22-CA237857-01A1); D.R.T., NIH Research Specialist Award (1R50CA243783); V.Q., NCI Emerging Questions in Cancer Systems Biology (U01 CA215845), NCI Research Centers for Cancer Systems Biology (U54 CA217450), NCI Predictive Multiscale Models for Biomedical, Biological, Behavioral, Environmental and Clinical Research (U01 CA174706), and Quantitative Systems Biology Center at Vanderbilt University.

COMPETING INTERESTS

The authors declare no competing interests.

AUTHOR CONTRIBUTIONS

Conceptualization, C.E.H., L.A.H., and V.Q.; Investigation and experiments, A.A., B.B.P., C.E.H., D.R.T., K.E.J., P.E.S.; Bioinformatic Analysis, B.B, C.E.H.; Modeling, C.E.H. and L.A.H.; Writing, B.B., C.E.H. and V.Q.; Review and Editing, A.B., B.B., C.E.H., L.A.H., and V.Q.

796 REFERENCES

797 1 Liu J, Dang H, Wang XW. The significance of intertumor and intratumor heterogeneity in
798 liver cancer. *Exp Mol Med* 2018; **50**: e416.
799 2 Inde Z, Dixon SJ. The impact of non-genetic heterogeneity on cancer cell death. *Crit Rev*
800 *Biochem Mol Biol* 2018; **53**: 99–114.
801 3 Hayford CE, Tyson DR, Robbins CJ, Frick PL, Quaranta V, Harris LA. An in vitro model of
802 tumor heterogeneity resolves genetic, epigenetic, and stochastic sources of cell state
803 variability. *PLOS Biol* 2021; **19**: e3000797.
804 4 Huang S. Genetic and non-genetic instability in tumor progression: link between the
805 fitness landscape and the epigenetic landscape of cancer cells. *Cancer Metastasis Rev*
806 2013; **32**: 423–448.
807 5 Brock A, Chang H, Huang S. Non-genetic heterogeneity--a mutation-independent driving
808 force for the somatic evolution of tumours. *Nat Rev Genet* 2009; **10**: 336–42.
809 6 Pisco AO, Huang S. Non-genetic cancer cell plasticity and therapy-induced stemness in
810 tumour relapse: 'What does not kill me strengthens me'. *Br J Cancer* 2015; **112**: 1725–
811 1732.
812 7 Paudel BB, Harris LA, Hardeman KN, Abugable AA, Hayford CE, Tyson DR *et al.* A
813 nonquiescent 'idling' population state in drug-treated, BRAF-mutated melanoma.
814 *Biophys J* 2018; **114**: 1499–1511.
815 8 Aranda-Anzaldo A, Dent MAR. Landscaping the epigenetic landscape of cancer. *Prog*
816 *Biophys Mol Biol* 2018; **140**: 155–174.
817 9 Sharma S V, Lee DY, Li B, Quinlan MP, Takahashi F, Maheswaran S *et al.* A chromatin-
818 mediated reversible drug-tolerant state in cancer cell subpopulations. *Cell* 2010; **141**: 69–
819 80.
820 10 Hata AN, Niederst MJ, Archibald HL, Gomez-Caraballo M, Siddiqui FM, Mulvey HE *et al.*
821 Tumor cells can follow distinct evolutionary paths to become resistant to epidermal
822 growth factor receptor inhibition. *Nat Med* 2016; **22**: 262–269.
823 11 Ramirez M, Rajaram S, Steininger RJ, Osipchuk D, Roth MA, Morinishi LS *et al.* Diverse
824 drug-resistance mechanisms can emerge from drug-tolerant cancer persister cells. *Nat*
825 *Commun* 2016; **7**: 10690.
826 12 Oren Y, Tsabar M, Cuoco MS, Amir-Zilberstein L, Cabanos HF, Hütter J-C *et al.* Cycling
827 cancer persister cells arise from lineages with distinct programs. *Nat 2021 5967873* 2021;
828 **596**: 576–582.
829 13 Jia D, Paudel BB, Hayford CE, Hardeman KN, Levine H, Onuchic JN *et al.* Drug-tolerant
830 idling melanoma cells exhibit theory-predicted metabolic low-low phenotype. *Front*
831 *Oncol* 2020; **10**: 1426.
832 14 Workman P, Travers J. Cancer: drug-tolerant insurgents. *Nature* 2010; **464**: 844–5.
833 15 Gutierrez C, Al'Khafaji AM, Brenner E, Johnson KE, Gohil SH, Lin Z *et al.* Multifunctional
834 barcoding with ClonMapper enables high-resolution study of clonal dynamics during
835 tumor evolution and treatment. *Nat Cancer 2021 27* 2021; **2**: 758–772.
836 16 Becht E, McInnes L, Healy J, Dutertre CA, Kwok IWH, Ng LG *et al.* Dimensionality
837 reduction for visualizing single-cell data using UMAP. *Nat Biotechnol* 2019; **37**: 38–47.
838 17 Xie Y, Hou W, Song X, Yu Y, Huang J, Sun X *et al.* Ferroptosis: process and function. *Cell*
839 *Death Differ* 2016; **23**: 369–379.

840 18 Boumahdi S, de Sauvage FJ. The great escape: tumour cell plasticity in resistance to
841 targeted therapy. *Nat Rev Drug Discov 2019 191* 2019; **19**: 39–56.
842 19 Gupta PB, Pastushenko I, Skibinski A, Blanpain C, Kuperwasser C. Phenotypic plasticity:
843 driver of cancer initiation, progression, and therapy resistance. *Cell Stem Cell* 2019; **24**:
844 65–78.
845 20 Rees M, Jessica C, Metcalf E, Childs DZ. Bet-hedging as an evolutionary game: the trade-
846 off between egg size and number. *Proc Biol Sci* 2010; **277**: 1149–51.
847 21 Jolly MK, Kulkarni P, Weninger K, Orban J, Levine H. Phenotypic plasticity, bet-hedging,
848 and androgen independence in prostate cancer: Role of non-genetic heterogeneity.
849 Front. Oncol. 2018; **8**: 50.
850 22 Shaffer SM, Dunagin MC, Torborg SR, Torre EA, Emert B, Krepler C *et al.* Rare cell
851 variability and drug-induced reprogramming as a mode of cancer drug resistance. *Nature*
852 2017; **546**: 431–435.
853 23 Emert BL, Cote CJ, Torre EA, Dardani IP, Jiang CL, Jain N *et al.* Variability within rare cell
854 states enables multiple paths toward drug resistance. *Nat Biotechnol 2021 397* 2021; **39**:
855 865–876.
856 24 Gray JW, Mills GB. Large-Scale Drug Screens Support Precision Medicine. *Cancer Discov*
857 2015; **5**: 1130–2.
858 25 Huang S, Kauffman S. How to escape the cancer attractor: Rationale and limitations of
859 multi-target drugs. *Semin Cancer Biol* 2013; **23**: 270–278.
860 26 Lee MJ, Ye AS, Gardino AK, Heijink AM, Sorger PK, MacBeath G *et al.* Sequential
861 application of anticancer drugs enhances cell death by rewiring apoptotic signaling
862 networks. *Cell* 2012; **149**: 780–94.
863 27 Hardeman KN, Peng C, Paudel BB, Meyer CT, Luong T, Tyson DR *et al.* Dependence on
864 glycolysis sensitizes BRAF-mutated melanomas for increased response to targeted BRAF
865 inhibition. *Sci Rep* 2017; **7**: 42604.
866 28 DeTomaso D, Jones MG, Subramaniam M, Ashuach T, Ye CJ, Yosef N. Functional
867 interpretation of single cell similarity maps. *Nat Commun* 2019; **10**: 4376.
868 29 Love MI, Huber W, Anders S. Moderated estimation of fold change and dispersion for
869 RNA-seq data with DESeq2. *Genome Biol* 2014; **15**: 1–21.
870

Figure 1

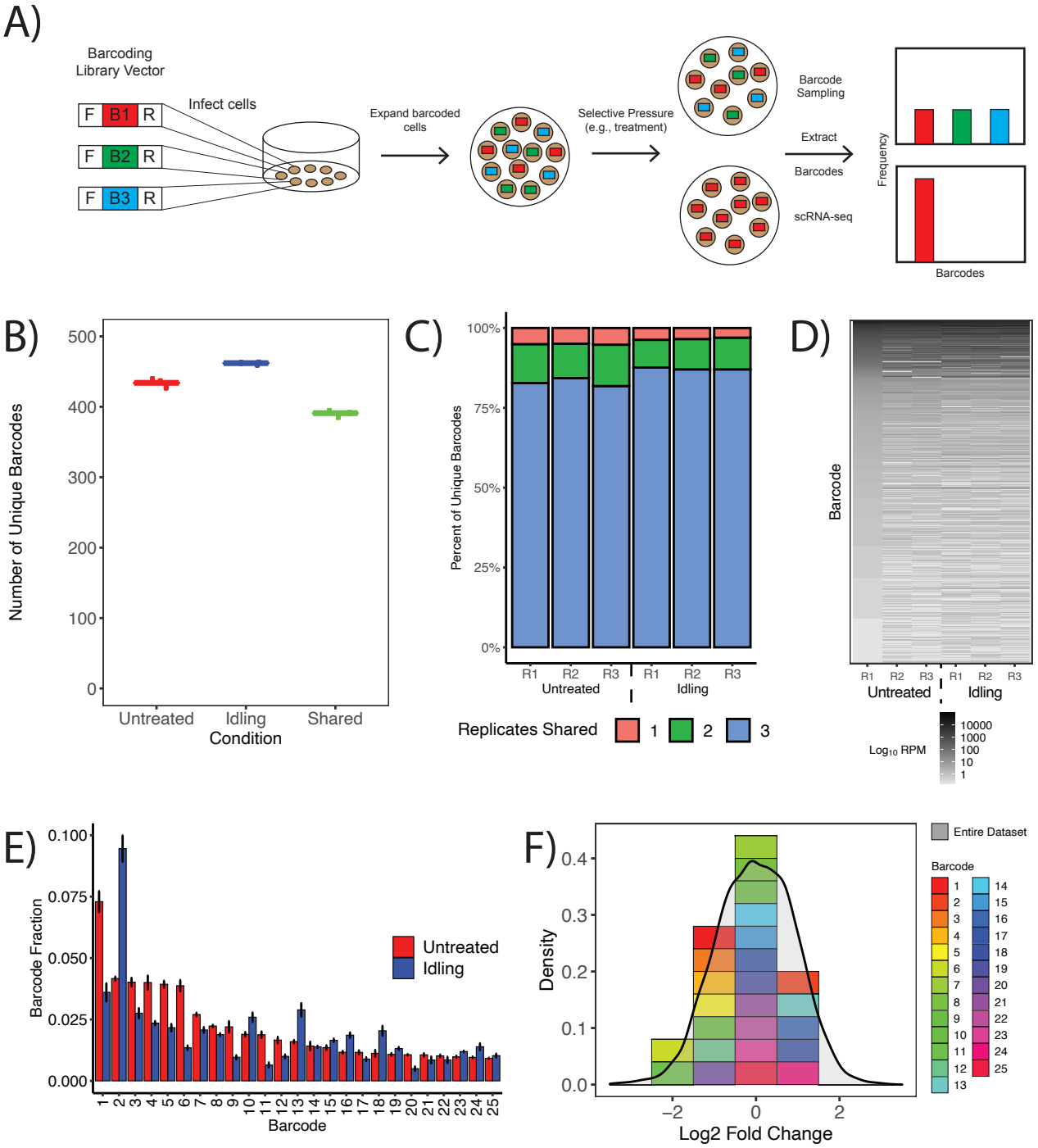
A)
Barcoding Library Vector
F B1 R
F B2 R
F B3 R
Infect cells
Expand barcoded cells
Selective Pressure (e.g., treatment)
Barcode Sampling
Extract
Barcodes
scRNA-seq
Frequency
Barcodes
B)
Number of Unique Barcodes
Untreated
Idling
Shared
Condition
C)
Percent of Unique Barcodes
Untreated
Idling
Replicates Shared
D)
Barcode
Untreated
Idling
Log10 RPM
E)
Barcode Fraction
Untreated
Idling
Barcode
F)
Density
Entire Dataset
Barcode
Log2 Fold Change

Figure 2

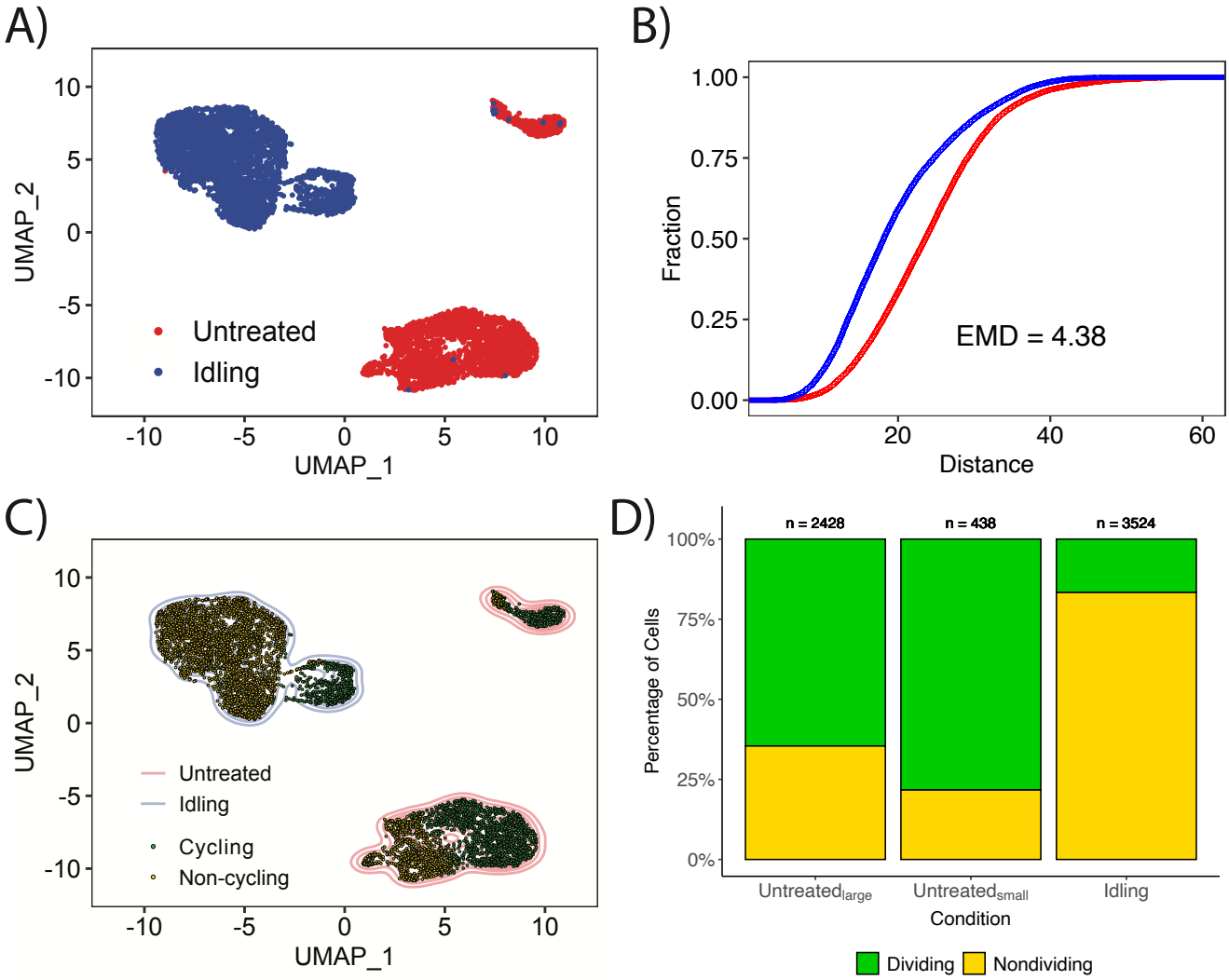
A)
UMAP_2
UMAP_1
Untreated
Idling
B)
Fraction
Distance
EMD = 4.38
C)
UMAP_2
UMAP_1
Untreated
Idling
Cycling
Non-cycling
D)
n = 2428
n = 438
n = 3524
Percentage of Cells
Condition
Untreated$_{large}$
Untreated$_{small}$
Idling
Dividing
Nondividing

Figure 3

A)

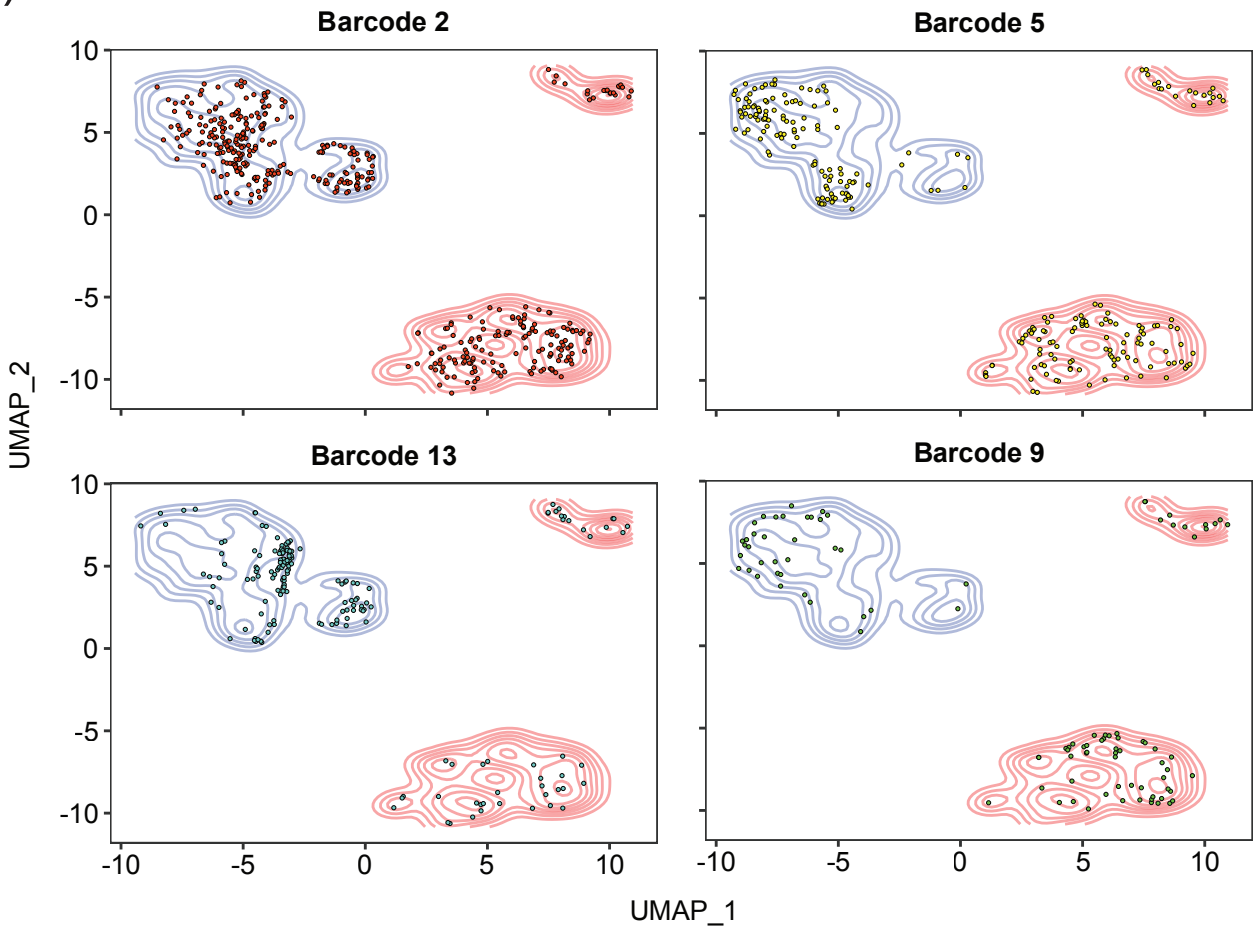
Barcode 2
Barcode 5
Barcode 13
Barcode 9
UMAP_2
UMAP_1
10
5
0
-5
-10

B)

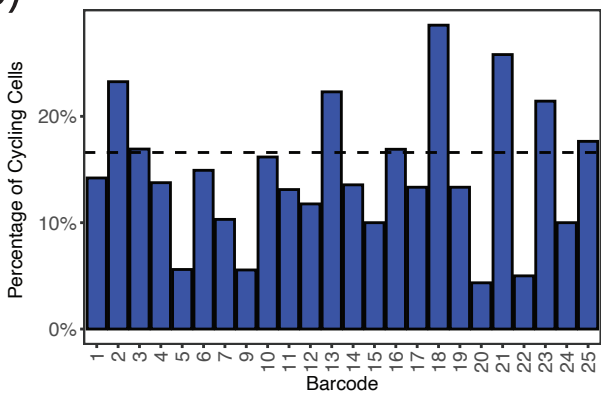
Percentage of Cycling Cells
20%
10%
0%
1 2 3 4 5 6 7 9 10 11 12 13 14 15 16 17 18 19 20 21 22 23 24 25
Barcode

C)

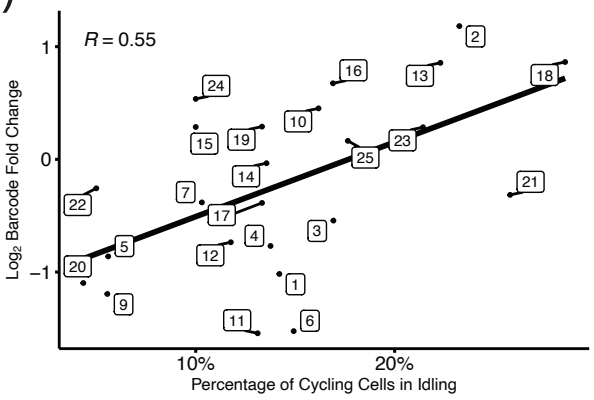
R = 0.55
Log2 Barcode Fold Change
1
0
−1
10%
20%
Percentage of Cycling Cells in Idling

Figure 4

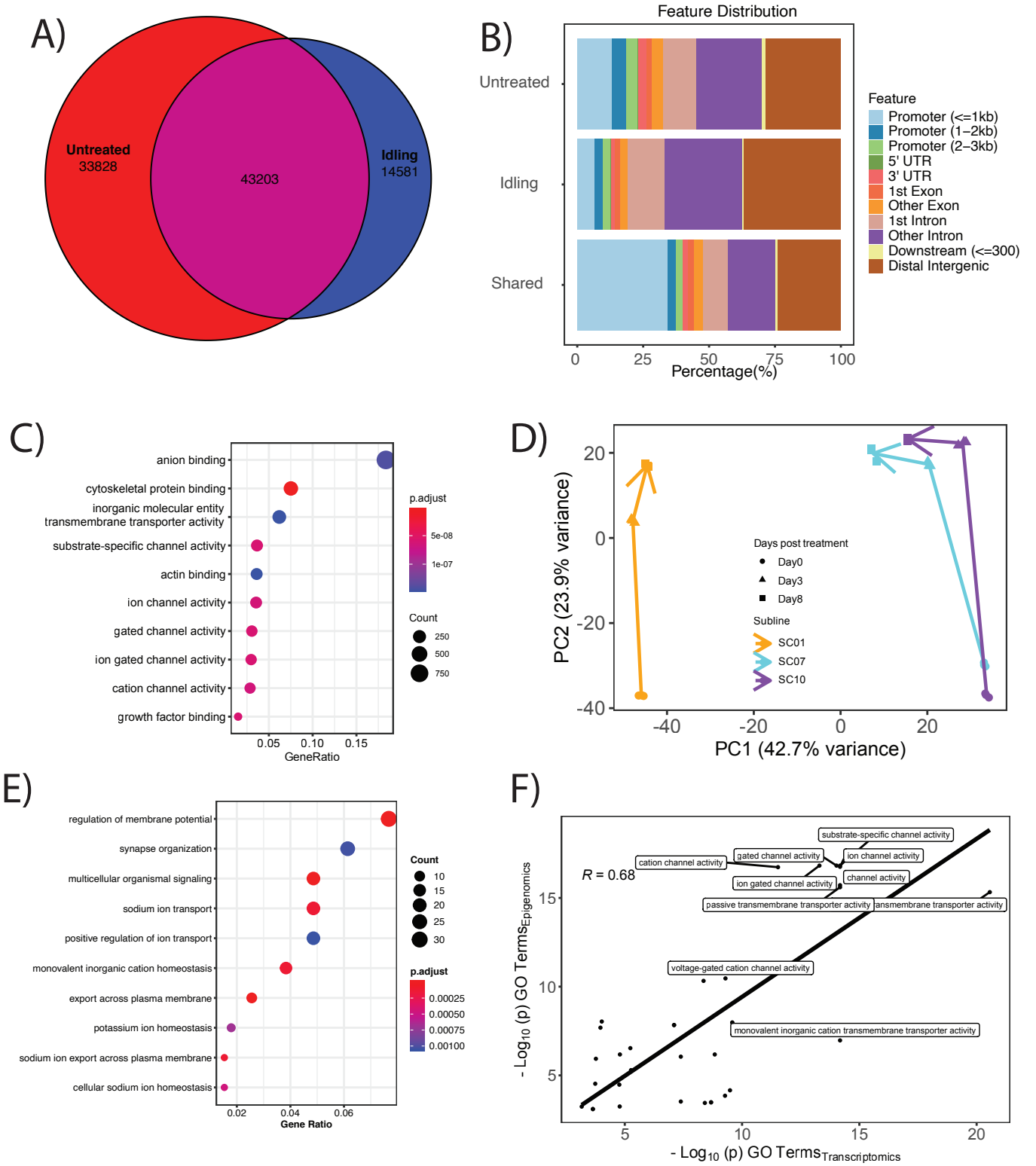
A)
Untreated
33828
43203
Idling
14581
B)
Feature Distribution
Untreated
Idling
Shared
0
25
50
75
100
Percentage(%)
Feature
Promoter (<=1kb)
Promoter (1−2kb)
Promoter (2−3kb)
5' UTR
3' UTR
1st Exon
Other Exon
1st Intron
Other Intron
Downstream (<=300)
Distal Intergenic
C)
anion binding
cytoskeletal protein binding
inorganic molecular entity transmembrane transporter activity
substrate-specific channel activity
actin binding
ion channel activity
gated channel activity
ion gated channel activity
cation channel activity
growth factor binding
0.05
0.10
0.15
GeneRatio
p.adjust
5e-08
1e-07
Count
250
500
750
D)
PC2 (23.9% variance)
PC1 (42.7% variance)
20
0
-20
-40
Days post treatment
Day0
Day3
Day8
Subline
SC01
SC07
SC10
E)
regulation of membrane potential
synapse organization
multicellular organismal signaling
sodium ion transport
positive regulation of ion transport
monovalent inorganic cation homeostasis
export across plasma membrane
potassium ion homeostasis
sodium ion export across plasma membrane
cellular sodium ion homeostasis
0.02
0.04
0.06
Gene Ratio
Count
10
15
20
25
30
p.adjust
0.00025
0.00050
0.00075
0.00100
F)
R = 0.68
substrate-specific channel activity
cation channel activity
gated channel activity
ion channel activity
channel activity
ion gated channel activity
passive transmembrane transporter activity
transmembrane transporter activity
voltage-gated cation channel activity
monovalent inorganic cation transmembrane transporter activity
- Log10 (p) GO Terms Epigenomics
- Log10 (p) GO Terms Transcriptomics
5
10
15
20

Figure 5

A)

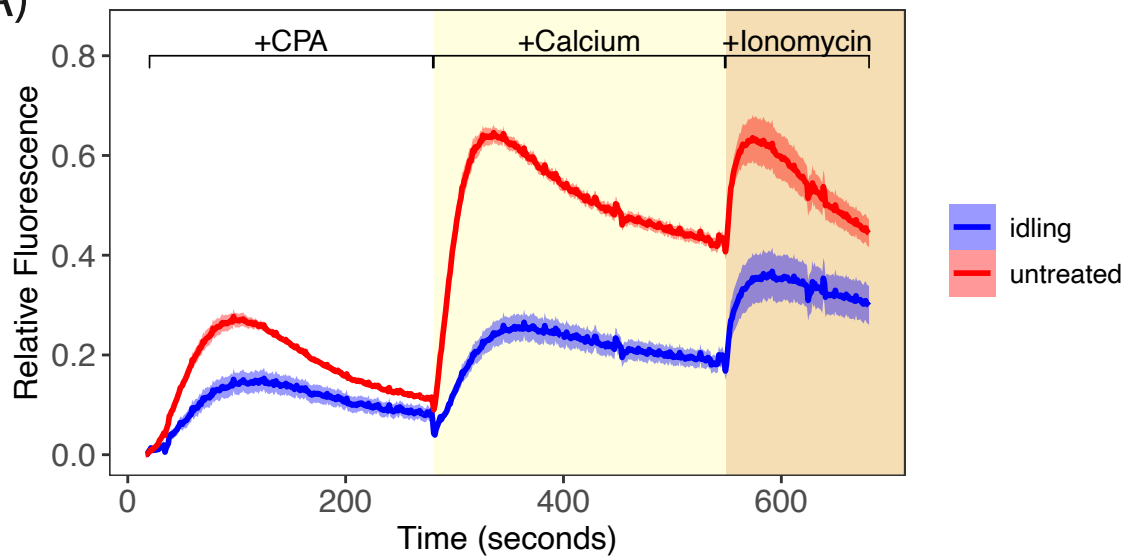
+CPA
+Calcium
+Ionomycin
Relative Fluorescence
0.0
0.2
0.4
0.6
0.8
0
200
400
600
Time (seconds)
idling
untreated

B)

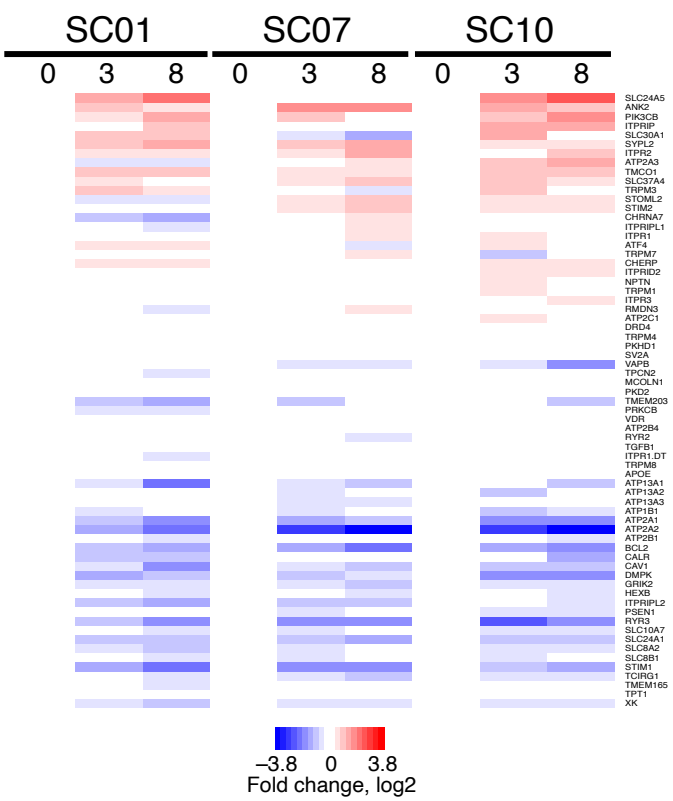
SC01
SC07
SC10
0 3 8
0 3 8
0 3 8
SLC24A5
ANK2
PIK3CB
ITPRIP
SLC30A1
SYPL2
ITPR2
ATP2A3
TMCO1
SLC37A4
TRPM3
STOML2
STIM2
CHRNA7
ITPRIPL1
ITPR1
ATF4
TRPM7
CHERP
ITPRID2
NPTN
TRPM1
ITPR3
RMDN3
ATP2C1
DRD4
TRPM4
PKHD1
SV2A
VAPB
TPCN2
MCOLN1
PKD2
TMEM203
PRKCB
VDR
ATP2B4
RYR2
TGFB1
ITPR1.DT
TRPM8
APOE
ATP13A1
ATP13A2
ATP13A3
ATP1B1
ATP2A1
ATP2A2
ATP2B1
BCL2
CALR
CAV1
DMPK
GRIK2
HEXB
ITPRIPL2
PSEN1
RYR3
SLC10A7
SLC24A1
SLC8A2
SLC8B1
STIM1
TCIRG1
TMEM165
TPT1
XK
–3.8 0 3.8
Fold change, log2

Figure 6

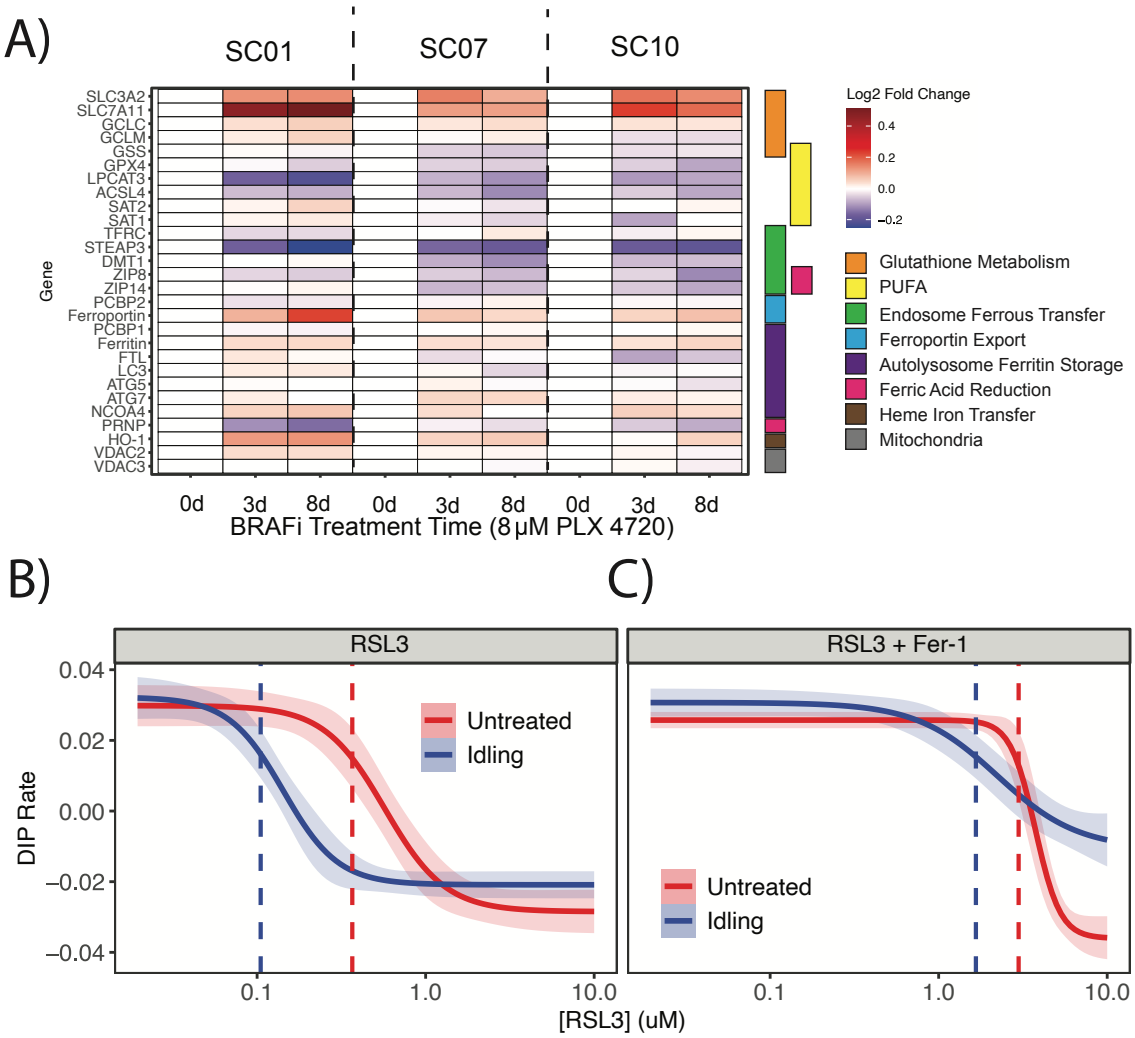
A)
SC01
SC07
SC10
Gene
SLC3A2
SLC7A11
GCLC
GCLM
GSS
GPX4
LPCAT3
ACSL4
SAT2
SAT1
TFRC
STEAP3
DMT1
ZIP8
ZIP14
PCBP2
Ferroportin
PCBP1
Ferritin
FTL
LC3
ATG5
ATG7
NCOA4
PRNP
HO-1
VDAC2
VDAC3
0d 3d 8d 0d 3d 8d 0d 3d 8d
BRAFi Treatment Time (8 μM PLX 4720)
Log2 Fold Change
0.4
0.2
0.0
−0.2
Glutathione Metabolism
PUFA
Endosome Ferrous Transfer
Ferroportin Export
Autolysosome Ferritin Storage
Ferric Acid Reduction
Heme Iron Transfer
Mitochondria
B)
C)
RSL3
RSL3 + Fer-1
DIP Rate
0.04
0.02
0.00
−0.02
−0.04
Untreated
Idling
0.1
1.0
10.0
[RSL3] (uM)